ARTICLES
https://doi.org/10.1038/s41563-018-0265-4
nature materials

Anti-resonance features of destructive quantum interference in single-molecule thiophene junctions achieved by electrochemical gating

Jie Bai[1,5], Abdalghani Daaoub[2,5], Sara Sangtarash[2,5], Xiaohui Li[1,5], Yongxiang Tang[1], Qi Zou[3], Hatef Sadeghi[2], Shuai Liu[1], Xiaojuan Huang[1], Zhibing Tan[1], Junyang Liu[1], Yang Yang[1], Jia Shi[1], Gábor Mészáros[4], Wenbo Chen[3*], Colin Lambert[2*] and Wenjing Hong[1*]

Controlling the electrical conductance and in particular the occurrence of quantum interference in single-molecule junctions through gating effects has potential for the realization of high-performance functional molecular devices. In this work we used an electrochemically gated, mechanically controllable break junction technique to tune the electronic behaviour of thiophene-based molecular junctions that show destructive quantum interference features. By varying the voltage applied to the electrochemical gate at room temperature, we reached a conductance minimum that provides direct evidence of charge transport controlled by an anti-resonance arising from destructive quantum interference. Our molecular system enables conductance tuning close to two orders of magnitude within the non-faradaic potential region, which is significantly higher than that achieved with molecules not showing destructive quantum interference. Our experimental results, interpreted using quantum transport theory, demonstrate that electrochemical gating is a promising strategy for obtaining improved in situ control over the electrical performance of interference-based molecular devices.

The understanding of charge transport through molecular building blocks is essential for the design of functional electric materials and devices from the molecular level. Charge transport at the nanoscale is dominated by quantum effects that can be controlled by the electron wavefunction. Among these effects, destructive quantum interference (DQI) in single-molecule junctions describes a quantum process in which the electron waves propagate through separated molecular orbitals and combine destructively[1–4]. This effect will lead to a reduction in the electron transmission probability and therefore a suppression of molecular conductance by orders of magnitude compared with molecular junctions without DQI[1,3]. Consequently, the control of DQI in single-molecule junctions offers a promising strategy for developing high-performance molecular devices such as molecular switches[5], transistors[6] and thermoelectric devices[7]. In previous works, efforts for controlling DQI utilized chemical design to manipulate the molecular architectures, including electronic structure modification[8], molecular topologies[9], heteroatom substitution[10] and even chemical reactions to change the molecular structures[11]. However, such indirect methods do not allow flexible and in situ control, and the fine tuning of interference remains a major challenge for the fabrication of interference-based molecular devices such as single-molecule transistors.

Although electrostatic gating offers an integrative approach for the tuning of the relative positions of molecule orbitals at different temperatures[12,13], electrochemical gating provides a complementary and effective approach to manipulate charge transport in the electrochemically active or inert molecular junctions at room temperature[14–17]. When the applied electrode potential varies in a non-faradaic region, the molecular energy alignment relative to the electrode Fermi energy is tuned[18], which offers in situ fine-tuning of charge transport through single-molecule junctions. Since the quantum interference in the charge transport through single-molecule junctions is energy-dependent, continuous tuning of the electrode potential offers an ideal strategy for realizing interference-based single-molecule electrochemical transistors (ECTs)[16–22], and the high gating efficiency and relatively large gate voltage windows provide opportunities for gating single-molecule junctions between resonances associated with molecular energy levels and anti-resonances associated with DQI[18,23].

Here, we develop a mechanically controllable break junction (MCBJ) technique chip integrated with an electrochemical gate for the fabrication of single-molecule ECTs in ionic liquid, and investigate charge transport through single-molecule thiophene junctions with DQI controlled by electrochemical gating. We observe the anti-resonance from DQI in a non-faradaic region at around −0.4 V versus a Ag/AgCl quasi-reference electrode, which offers direct evidence that charge transport is controlled by DQI. It is also found that the single-molecule thiophene junctions with DQI show a conductance enhancement of ~100× as the potential moves positively, which is significantly larger than that without DQI. Density functional theory (DFT) calculations of the electrochemical double layers around the molecular backbones confirm that the gating shifts the DQI anti-resonance feature towards the Fermi energy.

The measurements of single-molecule conductance were carried out on an electrochemical tip-bead (ECTB) chip integrated

[1]State Key Laboratory of Physical Chemistry of Solid Surfaces, iChEM, College of Chemistry and Chemical Engineering & Pen-Tung Sah Institute of Micro-Nano Science and Technology, Xiamen University, Xiamen, China. [2]Department of Physics, Lancaster University, Lancaster, UK. [3]Shanghai Key Laboratory of Materials Protection and Advanced Materials in Electric Power, Shanghai University of Electric Power, Shanghai, China. [4]Institute of Materials and Environmental Chemistry, Research Centre for Natural Sciences, Hungarian Academy of Sciences, Budapest, Hungary. [5]These authors contributed equally: Jie Bai, Abdalghani Daaoub, Sara Sangtarash, Xiaohui Li. *e-mail: wenbochen@shiep.edu.cn; c.lambert@lancaster.ac.uk; whong@xmu.edu.cn

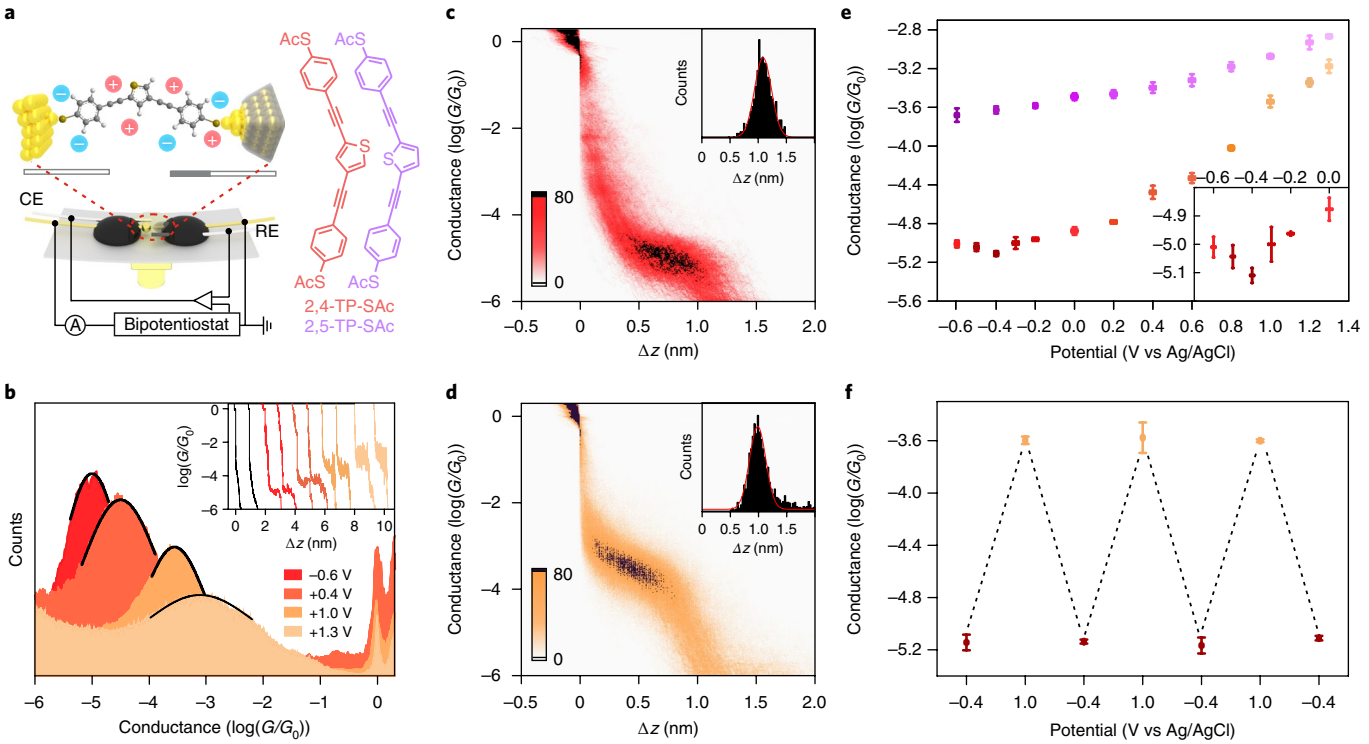

Fig. 1 | Electrochemical gating of 2,4-TP-SAc molecular junctions. a, Schematics of the electrochemically gated MCBJ technique and molecular structures of thiophene derivatives with anchoring groups of thioacetyl (-SAc). **b**, 1D conductance histograms of **2,4-TP-SAc** at different potentials, and the potentials of the coated Au tip relative to Ag/AgCl were chosen as the applied electrode potentials, while the potential of the Au beads was set to be 100 mV lower to obtain a bias of 100 mV between the two electrodes. Inset, typical individual traces of **2,4-TP-SAc** at different potentials: black, pure solvent; red, **2,4-TP-SAc** junctions at −0.6 V, orange at 0.4 V, yellow at 1.0 V and light yellow at 1.3 V. **c**,**d**, 2D conductance–displacement histograms of **2,4-TP-SAc** at −0.6 V (**c**) and 1.0 V (**d**), and the relative displacement distributions (insets). **e**, Tendency of the molecular conductance of **2,5-TP-SAc** (purple) and **2,4-TP-SAc** (orange) versus electrode potentials from −0.6 V to 1.3 V. Inset, magnification from −0.6 V to 0 V. **f**, Reversible switching of **2,4-TP-SAc** under sweep potentials between −0.4 V and 1.0 V. The error bars of the conductance value were determined from the variation of the most probable conductance values in three independent conductance measurements, and the error bars of the potential were determined from the potential stability test (Supplementary Fig. 2a).

with four electrodes for electrochemical gating using the MCBJ technique (Fig. 1a). The two working electrodes (source and drain electrodes), fabricated with a Au tip coated with insulating glue and a Au bead, were separated with a gap of ~20 μm and fixed on a stainless-steel sheet using epoxy resin. A Pt wire and a Ag wire coated with a layer of AgCl were introduced as the counter- and reference electrodes, respectively. This asymmetric architecture of the source and drain electrodes was taken from the scanning tunnelling microscopy break junction (STMBJ) method. This integrated electrochemical system on a MCBJ chip can be used for on-chip single-molecule ECTs. During the conductance measurements the gap between the two working electrodes was decreased until they were connected by bending the chip downwards (driven by a stepper motor and piezo stack), and this breaking/connecting process was repeated (see Supplementary Section 2 for details).

To reveal the role of DQI in the charge transport through a gated single-molecule junction, we investigated charge transport through thiophene core molecules with (**2,4-TP-SAc**) and without (**2,5-TP-SAc**) DQI, as shown in Fig. 1a. Figure 1b (inset) shows several typical individual stretching traces for **2,4-TP-SAc** with electrode potentials of −0.6 V, 0.4 V, 1.0 V and 1.3 V versus the reference potential. The black traces show tunnelling decay after the rupture of Au atomic contact in pure solvent, while molecular plateaus corresponding to the single-molecule conductance are found in the traces in solution with target molecules. The position of the molecular plateau shifts with the electrode potentials, suggesting the feasibility of electrochemical gating of single-molecule junctions using the MCBJ technique. In further analysis, hundreds to thousands of such conductance traces were used to construct the conductance histograms. Figure 1b shows one-dimensional (1D) conductance histograms of the **2,4-TP-SAc** molecule measured at different potentials. A pronounced conductance peak located at $10^{-5.0\pm0.03}G_0$ (conductance quantum, $G_0=2e^2/h$) was obtained for **2,4-TP-SAc** at −0.6 V, and shifted by almost two orders of magnitude to $10^{-3.2\pm0.07}G_0$ at 1.3 V. To exclude the conductance differences from configurational change, we constructed the 2D conductance–displacement histograms of **2,4-TP-SAc** at −0.6 V and 1.0 V, as shown in Fig. 1c,d. By accounting for the Au–Au snap back distance, the molecular length obtained from the relative stretched distance distribution was determined to be ~1.5 nm (1.0 nm determined from the relative displacement distribution, adding a Au–Au snap back distance of ~0.5 nm; ref. [24]). This is quite similar to the calculated molecular length, suggesting that the conductance enhancement can be ascribed to the applied electrode potentials rather than configurational change.

To reveal the variation of the molecular conductance with electrode potential within the whole non-faradaic region, we measured the molecular conductance while varying the electrode potentials from −0.6 V to 1.3 V, which is limited by desorption of the molecules at lower potential and Au oxidation at higher potential[25], as shown in Fig. 1e (see Supplementary Fig. 2 for cyclic voltammetry measurements). When electrochemical gating was applied, the molecular conductance increased by ~100× from $10^{-5.1\pm0.02}G_0$ at −0.4 V to $10^{-3.2\pm0.07}G_0$ at 1.3 V without a redox process. To further

investigate the role of DQI in electrochemically gated charge transport, we studied the conductance of **2,5-TP-SAc** without DQI (see Supplementary Fig. 5 for details), which increases by only 8× from $10^{-3.8\pm0.07}G_0$ at −0.6 V to $10^{-2.9\pm0.02}G_0$ at 1.3 V, indicating that **2,4-TP-SAc** junctions with DQI provide more than one order of magnitude higher conductance tuning than **2,5-TP-SAc** junctions without DQI.

More importantly, it is found that the molecular conductance at −0.6 V ($10^{-5.0\pm0.03}G_0$) is higher than that at −0.4 V ($10^{-5.1\pm0.02}G_0$). To verify this tendency, we carried out further experiments and plotted the molecular conductance at −0.3 V and −0.5 V (Fig. 1e, inset). Both conductance values at −0.3 V and −0.5 V are slightly higher than that at −0.4 V, but lower than those at −0.2 V and −0.6 V. Control experiments revealed that the conductance increase is not from the increase in Faradaic current (Supplementary Fig. 7). The observation is in accordance with the anti-resonance tendency of DQI with the minimum conductance at around −0.4 V. This is a direct evidence of the tuning of the anti-resonance of DQI. Previous work has suggested that the transmission functions of molecular junctions could be mapped electrochemically[23]. Here, we also demonstrate that the DQI can be directly mapped through electrochemical gating at room temperature.

The high gating efficiency of **2,4-TP-SAc** leads to the fabrication of high-performance single-molecule ECTs. Figure 1f presents the reversible switching cycles of **2,4-TP-SAc** under sweep potentials between −0.4 V and 1.0 V. It is found that the conductance changes with potential without any attenuation in conductance ratio. The large variation of the conductance provides a promising way to construct the molecular switch based on DQI, which tunes the electrode Fermi energy between the near-resonance state and the anti-resonance state.

To further confirm the potential-dependent variation in conductance we carried out conductance–potential measurements for **2,4-TP-SAc** and **2,5-TP-SAc** in the same environmental conditions, with electrochemically gated conductance measurements (see Methods for details). As shown in Fig. 2a,b, there is a clear drop at around −0.4 V in most of the individual conductance–electrode potential traces from the measurement of **2,4-TP-SAc**, while most of the traces of **2,5-TP-SAc** show increases with gate voltage from −0.6 V to −0.2 V. It is found that the current determined from the conductance–electrode potential measurement is slightly lower than that from the electrochemically gated conductance measurement, which may arise from the preferred fully stretched molecular configuration[24] as well as a contribution from the Faradaic discharging current. Notably, the conductance drop in individual traces is found to be around half an order of magnitude, which is even higher than that determined from the electrochemically gated conductance measurement. All data plots shown in Fig. 2c demonstrated the presence of a clear V-shaped node with a minimum at around −0.38 V for **2,4-TP-SAc**, which agrees well with the electrochemically gated conductance measurement and offers direct evidence of anti-resonance from DQI. In contrast, the conductance–electrochemical potential traces of **2,5-TP-SAc** show a slight increase, shown in Fig. 2d.

We also carried out current/conductance–voltage measurements at different potentials by sweeping the bias continuously between −1.0 V and +1.0 V at a sweeping rate of 5 V s^{-1} (refs. [24,26,27]). Hundreds of current/conductance–voltage traces with molecular junctions are plotted in a 2D conductance–gate voltage histogram; typical conductance–gate voltage traces at −0.4 V are shown in Fig. 2e, which exhibit a significant voltage dependence. We compared the most probable current/conductance–voltage traces at different potentials, and found that the current/conductance–voltage curves remained almost constant at 1.0 V for the molecules, suggesting that the Fermi levels are far from resonance or anti-resonance. More interestingly, it was found that the current/conductance–gate voltage at −0.6 V is even more tilted than that at −0.4 V. When we analysed the conductance distributions in current/conductance–voltage traces for slopes from −100 mV to 100 mV, the most probable conductances were determined to be $10^{-4.9\pm0.4}G_0$ at −0.6 V, $10^{-5.0\pm0.5}G_0$ at −0.4 V, $10^{-4.4\pm0.5}G_0$ at 0.6 V and $10^{-3.5\pm0.5}G_0$ at 1.0 V for **2,4-TP-SAc**, which agree well with the conductance measurements at fixed bias voltage (see Supplementary Fig. 8 for the measurements for **2,5-TP-SAc**).

To verify the generality of this strategy and to study the role of electrode–molecule coupling, we replaced the anchoring group –SAc with –SMe and investigated the single-molecule conductance under electrochemical gating (Fig. 3). It was found that the molecular conductance of **2,4-TP-SMe** increased by ~20× from −0.2 V to 1.0 V, compared with an ~4× increase for **2,5-TP-SMe** (see Supplementary Fig. 8 for details). This tendency is similar to that of **2,4-TP-SAc**, except that the –SMe will desorb from Au when the electrode potential is more negative than −0.2 V (refs. [16,23]), which prevents the formation of a molecular junction at their anti-resonance states. Comparing the conductance variation of **2,4-TP-SMe** (20×) and **2,4-TP-SAc** (27×) in the potential range from −0.2 V to 1.0 V, reduction of the electrode–molecule coupling from the covalent Au–S bond to the coordinating Au–SMe bond does not provide more effective conductance tuning of the single-molecule junctions on varying the electrode potential.

To understand the effect of electrochemical gating on single-molecule junctions we performed quantum transport calculations[28,29] on the junctions formed by thiophene cores with 2,4 and 2,5 connectivities to the Au electrodes via thiol or –SMe as anchoring group, both in the absence and presence of $HMIPF_6$ (HMI, 1-hexyl-3-methylimidazolium; see Methods and Supplementary Fig. 9). The transmission coefficient $T(E)$ of the bare junction in the absence of $HMIPF_6$ shows a clear DQI feature for **2,4-TP-SAc**, while **2,5-TP-SAc** shows no DQI features (Fig. 4b,c). When an electric field is applied, depending on the orientation of the $HMIPF_6$ the transmission coefficient shifts to the left or right. In Fig. 4, $d_x^{\pm}$ denotes the positions of $HMIPF_6$ with respect to the backbone as well as the potential orientation (d_x^- represents the position of $HMIPF_6$ with respect to the molecular backbone at negative potentials and d_x^+ represents the position of $HMIPF_6$ at positive potentials; x ranges from 1 to 5, corresponding to decreasing distance of $HMIPF_6$ from the molecular backbone; detailed distances are shown in Supplementary Fig. 9). When the HMI moiety is closer to the backbone (d_x^- in Fig. 4), $T(E)$ shifts to the left, whereas it shifts to the right when PF_6 gets closer to the backbone (d_x^+ in Fig. 4). It is found that the HOMO–LUMO gap also shrinks due to the electric field. In addition, the anti-resonance dip associated with DQI in **2,4-TP-SAc** is moved by the position of the $HMIPF_6$. Clearly, if the Fermi energy lies close to the anti-resonance of $T(E)$ in **2,4-TP-SAc**, a large variation of the conductance is predicted (red curves in Fig. 4b). Conversely, when the $HMIPF_6$ approaches the backbone from the PF_6 side, the dip in $T(E)$ moves to the right, away from the DFT-predicted Fermi energy (black dashed line), and the HOMO moves closer, which leads to near-resonance charge transport (yellow curves in Fig. 4b). In **2,5-TP-SAc** (Fig. 4c,d), $T(E)$ does not have a dip and therefore a smaller variation is predicted unless the Fermi energy happens to be in the tail of the resonances. Figure 4d shows the theoretical variation of the conductance versus the position of $HMIPF_6$ with respect to the backbone for both **2,4-TP-SAc** and **2,5-TP-SAc**. For **2,4-TP-SAc**, the conductance initially decreases with a negative field from d_1^- to d_4^-, but then increases from d_4^- to d_5^-, suggesting the presence of an anti-resonance dip from the DQI effect at the d_4^- states, which originates from crossing of the DQI dip at the Fermi energy, as shown in Fig. 4b. It is also found that the HOMO moves closer at positive potentials, suggesting the presence of near-resonance charge transport, in agreement with the significant conductance increase of **2,4-TP-SAc** at positive potentials shown in Fig. 1e. The calculated conductance

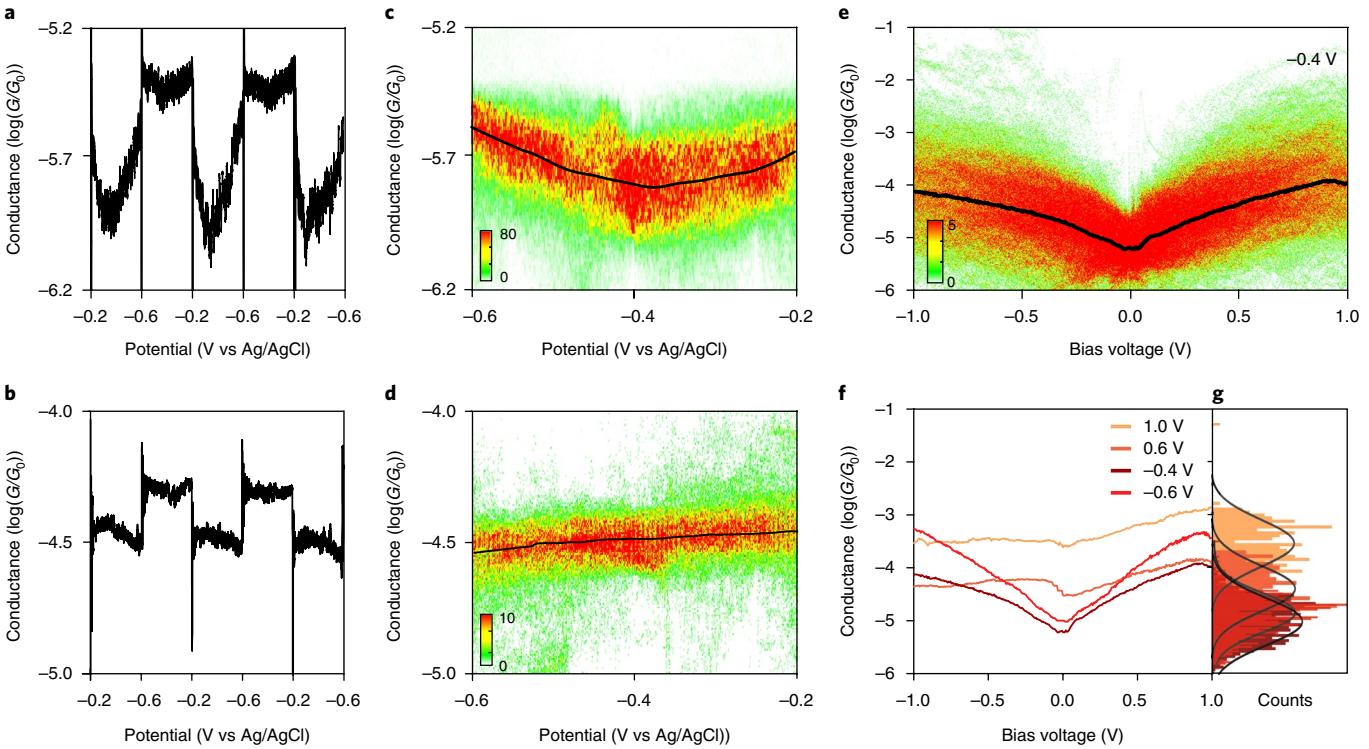

Fig. 2 | Conductance–electrode potential and current/conductance–voltage measurements of 2,4-TP-SAc and 2,5-TP-SAc molecular junctions. **a**, Typical individual conductance–electrode potential traces of **2,4-TP-SAc**. **b**, Typical individual conductance–electrode potential traces of **2,5-TP-SAc**. **c**, 2D histogram of conductance–electrode potential of **2,4-TP-SAc** (503 traces). **d**, 2D histogram of conductance–electrode potential of **2,5-TP-SAc** (184 traces). **e**, 2D histogram and the most probable curve of current/conductance–voltage of **2,4-TP-SAc** at −0.4 V (1,154 traces). **f**, Most probable traces from 2D histogram of current/conductance–voltage of **2,4-TP-SAc** at 1.0 V, 0.6 V, −0.4 V and −0.6 V. **g**, Conductance distributions of low-bias conductance determined from the slopes from −100 mV to 100 mV in current/conductance–voltage traces; count numbers are scaled for better comparison.

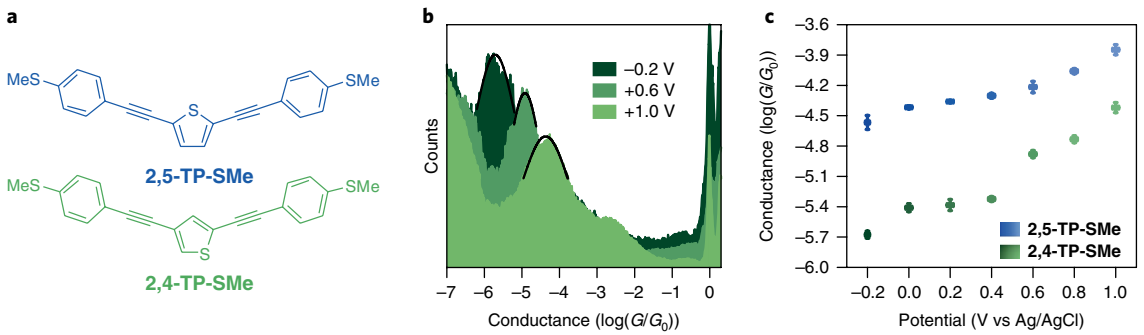

Fig. 3 | Transport characteristics of 2,4-TP-SMe and 2,5-TP-SMe molecular junctions. **a**, Molecular structures of thiophene derivatives with the anchoring group thiomethyl (-SMe). **b**, 1D conductance histograms of **2,4-TP-SMe** at different electrode potentials. **c**, Tendency of the molecular conductances of **2,4-TP-SMe** and **2,5-TP-SMe** versus electrode potentials from −0.2 to 1.0 V. The error bars for the conductance values are determined from variation of the most probable conductance values in three independent conductance measurements. The error bars of the potential are determined from the potential stability test (Supplementary Fig. 2a).

difference between anti-resonance (d_4^- state) and near-resonance (d_5^+ state) is determined to be around two orders of magnitude, which is quite close to the experimental ratio of ~100. In comparison, the conductance variation of **2,5-TP-SAc** is much smaller, which is ascribed to the absence of a DQI feature in the transmission of **2,5-TP-SAc**. We also calculated the conductance–voltage traces for **2,4-TP-SAc**, which qualitatively agree with the experimentally determined conductance–voltage traces, suggesting that gating towards anti-resonance leads to a more pronounced voltage dependence of the conductance at the d_4^- and d_5^- states. We can also conclude that the most tilted shape of the experimental conductance–voltage traces for **2,4-TP-SAc** at −0.6 V (d_5^- state) arises when the Fermi level is located between a resonance and anti-resonance, which leads to the sharpest transmission changes[24,26,27] (see Supplementary Section 5 for details).

In summary, we have employed electrochemical gating for the fine-tuning of charge transport properties in single-molecule thiophene junctions with and without DQI using a modified electrochemical MCBJ technique. Benefiting from the high gating efficiency of electrochemical gating and the large potential windows

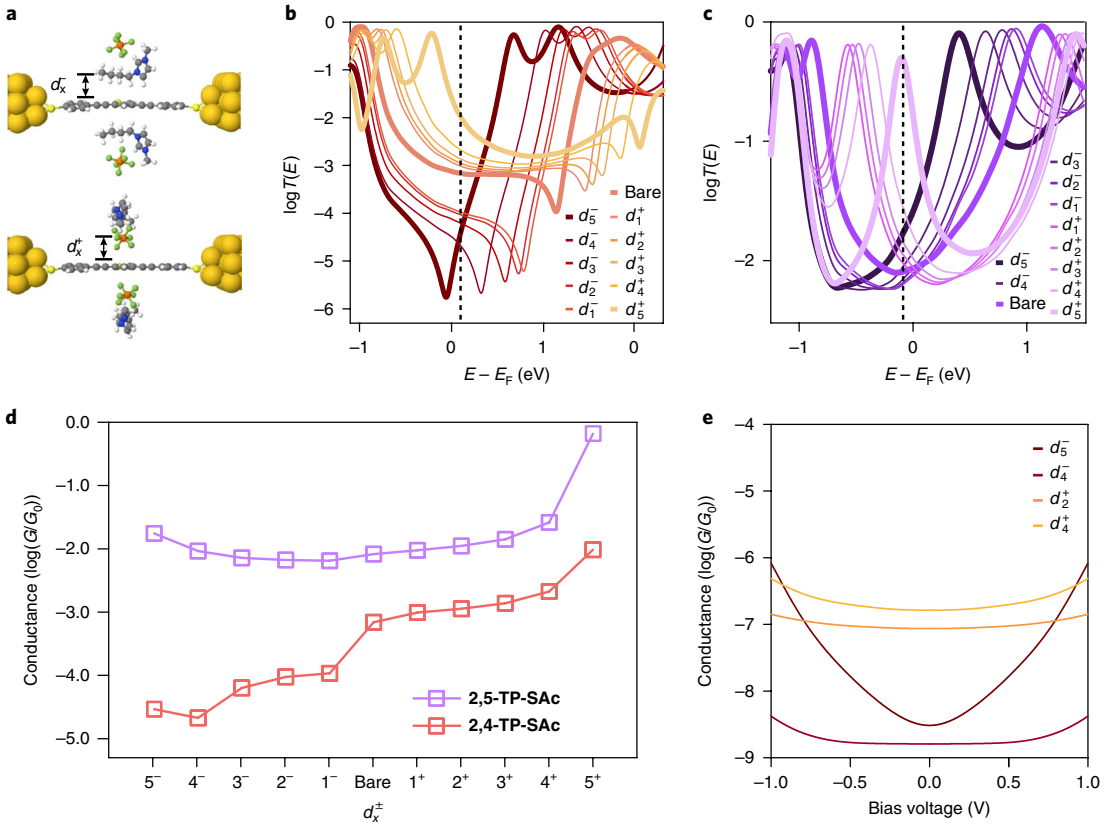

Fig. 4 | Transport properties of thiophene core molecular junctions in the absence and presence of $HMIPF_6$. **a**, Structure of **2,4-TP-SAc** molecular junctions under negative (top) and positive (bottom) potential. **b**, Transmission coefficients of **2,4-TP-SAc** in the presence of negative and positive charges at different positions. **c**, Transmission coefficients of **2,5-TP-SAc** in the presence of negative and positive charges at different positions. **d**, Comparison of **2,4-TP-SAc** and **2,5-TP-SAc** conductance versus position of $HMIPF_6$. The Fermi energy (black dashed lines) lies around the middle of the highest occupied molecular orbital and lowest unoccupied molecular orbital (HOMO–LUMO) gap ($E_F = 0.1$ eV) of the bare junction for **2,4-TP-SAc** and at −0.08 eV for **2,5-TP-SAc**. **e**, Calculated conductance versus bias voltage of **2,4-TP-SAc** for different positions of $HMIPF_6$.

of ionic liquid, this work provides the experimental observation of charge transport at an anti-resonance state arising from DQI at room temperature, which is also supported by DFT simulations of the electrochemical double layer. It is found that the gating of single-molecule thiophene junctions with DQI when the Fermi level is located between a resonance and anti-resonance, shows ~100 times conductance variation by tuning the electrode potential from −0.4 V to 1.3 V versus the Ag/AgCl quasi-reference electrode in ionic liquid, which is more than one order of magnitude higher than that without DQI. The electrochemical tuning of DQI presented in this work provides a promising design strategy for tuning of interference in future molecular materials and devices.

Online content

Any methods, additional references, Nature Research reporting summaries, source data, statements of data availability and associated accession codes are available at https://doi.org/10.1038/s41563-018-0265-4.

Received: 7 August 2018; Accepted: 3 December 2018;
Published online: 11 February 2019

References

1. Guedon, C. M. et al. Observation of quantum interference in molecular charge transport. *Nat. Nanotech.* **7**, 305–309 (2012).
2. Lambert, C. J. Basic concepts of quantum interference and electron transport in single-molecule electronics. *Chem. Soc. Rev.* **44**, 875–888 (2015).
3. Garner, M. H. et al. Comprehensive suppression of single-molecule conductance using destructive σ-interference. *Nature* **558**, 415–419 (2018).
4. Frisenda, R., Janssen, V. A. E. C., Grozema, F. C., van der Zant, H. S. J. & Renaud, N. Mechanically controlled quantum interference in individual π-stacked dimers. *Nat. Chem.* **8**, 1099 (2016).
5. Baer, R. & Neuhauser, D. Phase coherent electronics: a molecular switch based on quantum interference. *J. Am. Chem. Soc.* **124**, 4200–4201 (2002).
6. Hsu, L. Y. & Rabitz, H. Single-molecule phenyl-acetylene-macrocycle-based optoelectronic switch functioning as a quantum-interference-effect transistor. *Phys. Rev. Lett.* **109**, 186801 (2012).
7. Bergfield, J. P., Solomon, G. C., Stafford, C. A. & Ratner, M. A. Novel quantum interference effects in transport through molecular radicals. *Nano Lett.* **11**, 2759–2764 (2011).
8. Manrique, D. Z. et al. A quantum circuit rule for interference effects in single-molecule electrical junctions. *Nat. Commun.* **6**, 6389 (2015).
9. Sangtarash, S. et al. Searching the hearts of graphene-like molecules for simplicity, sensitivity, and logic. *J. Am. Chem. Soc.* **137**, 11425–11431 (2015).
10. Liu, X. S. et al. Gating of quantum interference in molecular junctions by heteroatom substitution. *Angew. Chem. Int. Ed.* **56**, 173–176 (2017).
11. Huang, C. et al. Single-molecule detection of dihydroazulene photo-thermal reaction using break junction technique. *Nat. Commun.* **8**, 15436 (2017).
12. Song, H. et al. Observation of molecular orbital gating. *Nature* **462**, 1039–1043 (2009).
13. Perrin, M. L. et al. Large tunable image-charge effects in single-molecule junctions. *Nat. Nanotech.* **8**, 282 (2013).
14. Huang, C., Rudnev, A. V., Hong, W. & Wandlowski, T. Break junction under electrochemical gating: testbed for single-molecule electronics. *Chem. Soc. Rev.* **44**, 889–901 (2015).
15. Nichols, R. J. & Higgins, S. J. Single molecule nanoelectrochemistry in electrical junctions. *Acc. Chem. Res.* **49**, 2640–2648 (2016).
16. Capozzi, B. et al. Tunable charge transport in single-molecule junctions via electrolytic gating. *Nano Lett.* **14**, 1400–1404 (2014).
17. Xiang, L. et al. Gate-controlled conductance switching in DNA. *Nat. Commun.* **8**, 14471 (2017).

18. Baghernejad, M. et al. Highly-effective gating of single-molecule junctions: an electrochemical approach. *Chem. Commun.* **50**, 15975–15978 (2014).
19. Brooke, R. J. et al. Single-molecule electrochemical transistor utilizing a nickel-pyridyl spinterface. *Nano Lett.* **15**, 275–280 (2015).
20. Kay, N. J. et al. Single-molecule electrochemical gating in ionic liquids. *J. Am. Chem. Soc.* **134**, 16817–16826 (2012).
21. Ruiz, M. P. et al. Bioengineering a single-protein junction. *J. Am. Chem. Soc.* **139**, 15337–15346 (2017).
22. Ting, T.-C. et al. Energy-level alignment for single-molecule conductance of extended metal-atom chains. *Angew. Chem. Int. Ed.* **54**, 15734–15738 (2015).
23. Capozzi, B. et al. Mapping the transmission functions of single-molecule junctions. *Nano Lett.* **16**, 3949–3954 (2016).
24. Hong, W. et al. Single molecular conductance of tolanes: experimental and theoretical study on the junction evolution dependent on the anchoring group. *J. Am. Chem. Soc.* **134**, 2292–2304 (2012).
25. Li, J., Shen, Y., Zhang, Y. & Liu, Y. Room-temperature ionic liquids as media to enhance the electrochemical stability of self-assembled monolayers of alkanethiols on gold electrodes. *Chem. Commun.* **2005**, 360–362 (2005).
26. Guo, S., Hihath, J., Díez-Pérez, I. & Tao, N. Measurement and statistical analysis of single-molecule current–voltage characteristics, transition voltage spectroscopy, and tunneling barrier height. *J. Am. Chem. Soc.* **133**, 19189–19197 (2011).
27. Leary, E. et al. Detecting mechanochemical atropisomerization within an STM break junction. *J. Am. Chem. Soc.* **140**, 710–718 (2018).
28. Sadeghi, H. Theory of electron, phonon and spin transport in nanoscale quantum devices. *Nanotechnology* **29**, 373001 (2018).
29. Ferrer, J. et al. Gollum: a next-generation simulation tool for electron, thermal and spin transport. *New J. Phys.* **16**, 093029 (2014).

Acknowledgements

This research was supported by the National Key R&D Program of China (2017YFA0204902), the National Natural Science Foundation of China (21722305, 21673195, 21503179 and 21703188), the Program for Professor of Special Appointment (Eastern Scholar) at Shanghai Institutions of Higher Learning, the Natural Science Foundation of Shanghai (17ZR1447100), the Science and Technology Commission of Shanghai Municipality (14DZ2261000) and the China Postdoctoral Science Foundation (2017M622060) for funding work in Xiamen. It was also supported by EU Horizon 2020 project QuIET under grant agreement no. 767187 and UK EPSRC grants EP/N017188/1 and EP/M014452/1 and Leverhulme Trust (Leverhulme Early Career Fellowships no. ECF-2017-186 and ECF-2018-375) for funding instrumentation used in Lancaster. It was also supported by Hungarian and Czech Academies of Sciences (P2015-107) andHungarian Research Foundation (OTKA 112034) for funding instrumentation used in Hungary. The authors thank Z.-Q. Tian and B.-W. Mao, Xiamen University, for useful discussions.

Author contributions

W.H. and J.B. conceived the idea and designed the experiments. W.H., C.L. and W.C. co-supervised the project. J.B., W.H., A.D. and S.S. wrote the manuscript with input from all authors. J.B., X.L. and X.H. carried out the break junction experiments and analysed the data. Q.Z. and W.C. synthesized and provided the structural characterization of the molecules. J.B. and S.L. performed the cyclic voltammetry measurements. Y.T., G.M., J.S. and W.H. built the electrical measurement instrument and wrote the software to control the break junction set-up. A.D., S.S., C.L. and H.S. performed the theoretical modelling. Z.T., J.L. and Y.Y. revised the manuscript. All authors discussed the experiments.

Competing interests

The authors declare no competing interests.

Additional information

Supplementary information is available for this paper at https://doi.org/10.1038/s41563-018-0265-4.

Reprints and permissions information is available at www.nature.com/reprints.

Correspondence and requests for materials should be addressed to W.C. or C.L. or W.H.

Publisher's note: Springer Nature remains neutral with regard to jurisdictional claims in published maps and institutional affiliations.

Methods

Synthesis. The target molecules were prepared by the Sonogashira coupling of 4-ethynylthioanisole and 1-(thioacetyl)-4-ethynylbenzene with 2,5-dibromothiophene and 2,4-dibromothiophene, respectively. 4-Ethynylthioanisole and 1-(thioacetyl)-4-ethynylbenzene were prepared according to published procedures (Supplementary Section 1).

Chip fabrication. Materials for chip fabrication were prepared as follows. Ag/AgCl wire was fabricated by electrochemically oxidized Ag wire (0.1 mm diameter, 99.99%, Jiaming) at a constant potential of 1.5 V in electrolyte (37% HCl:H_2O = 1:1, vol/vol). The coated Au tip was prepared by etching Au wire (0.15 mm diameter, 99.99%, Jiaming) in a solution of 37% HCl:ethanol (1:1, vol/vol) at a potential of 1.2 V and then coating it with hot melt adhesive (Ace Hardware). Au beads of 0.35–0.50 mm in diameter were annealed by butane flame. The electrodes were fixed onto a sheet of spring steel (30 mm × 10 mm with 0.2 mm thickness) using two drops of epoxy (Stycast 2850 FT with catalyst 9).

The fabrication process for the ECTB chip was as follows. The spring steel sheets (30 mm × 10 mm × 0.2 mm) were cleaned with acetone and Milli-Q water, then dried by nitrogen flow. The coated Au tip wire and Pt wire (0.1 mm diameter, 99.95%) were fixed on the sheet with one drop of epoxy (mixture of Stycast 2850 FT epoxy resin and 3.5 wt% Catalyst 9). After complete polymerization at room temperature, the Au bead and Ag/AgCl wire were fixed on the other side of the sheet by one drop of epoxy. The initial distance between the coated Au tip and the Au bead was adjusted to be less than 50 μm under an optical microscope (SAIKEDIGITAL, SK2700U). Before the experiment, the as-prepared chip was rinsed by isopropanol and dried by natural volatilization.

Electrochemical measurements. CV measurements under ambient conditions were carried out with our laboratory-built bipotentiostat, while an Autolab electrochemical workstation (Eco Chemie) was used when measuring in a glovebox filled with ultra-pure argon.

The stability of the Ag/AgCl quasi-reference electrode was tested by open-circuit potential measurements using a two-electrode system[30]. The working electrode and the reference electrode were the Ag/AgCl quasi-reference electrode and a commercial saturated calomel electrode (SCE, CH Instruments), respectively. The two electrodes were set separately (the Ag/AgCl quasi-reference electrode was placed in the $HMIPF_6$ ionic liquid, and the SCE was placed in a saturated KCl aqueous solution) and connected through an agar-KNO_3-$HMIPF_6$-filled salt bridge. The potential signal outputs from the two electrodes were recorded using an Autolab electrochemical workstation (Eco Chemie).

Conductance measurements. Before the experiments, the as-prepared chip was rinsed in isopropanol and dried by natural volatilization. The chip was then installed with a polytetrafluoroethylene (PTFE) liquid cell on top, fixed by two Al alloy plates (see Supplementary Section 2 for details). The thiophene derivatives (see Supplementary Section 1 for the synthetic method and characterization) were prepared to be 0.5 mM in a solvent of $HMIPF_6$ (purchased from lolitec Ionic Liquids Technologies). During the single-molecule conductance measurements, 10–15 μL of molecular solution was added to the PTFE liquid cell.

The electrochemically gated MCBJ measurements were based on a laboratory-built bipotentiostat with a tunable logarithmic current–voltage converter[31]. During experiments, the bias voltage between two working electrodes (coated Au tip and Au bead) was fixed to be 0.1 V, and the current passing through the working electrodes was measured by a logarithmic I–V converter with a sampling rate of 10 kHz using a microcontroller for data acquisition. During the measurements, the ECTB chip was bent down and up with the Al alloy plates, which were driven by a combination of a stepper motor (Zaber NA14B16) and a piezo stack (Thorlab AE0505D18F). The evolution of the conductance characteristics was recorded for further analysis during the repeated connecting/breaking process. A statistical analysis was used to determine the conductance and stretching displacement distribution of the molecular junctions. The construction of 1D conductance histograms from typical individual traces provides a way to quantify the most probable conductance. To reveal the evolution process of the single-molecule junctions, 2D conductance–displacement histograms were constructed. The distance between the electrodes on the ECTB chip was determined from the tunnelling current as reported in our previous paper[24], and the relative displacement distributions were calibrated from the stretching rate determined from pure solvent measurements (see Supplementary Section 4.2 for details). In this case, the tunnelling decay constants in pure solvent and molecule-containing solution were considered to be the same to simplify the calibration, although the tunnelling decay constant varied after adding molecules into the solution.

Conductance–electrode potential measurements. The conductance–electrode potential measurements were carried out under the same environmental conditions as the electrochemically gated conductance measurements. Instead of the fixed potential in the electrochemically gated conductance measurements, the break junction experiment was started with a preset potential of −0.2 V. Once the conductance reached the conductance range of the molecular plateau (setting 4×10^{-5} μA for **2,4-TP-SAc** and 8×10^{-4} μA for **2,5-TP-SAc**), we used the microcontroller to keep the distance between the two electrodes at a certain value, and started to sweep the gate voltage from −0.2 V to −0.6 V at a rate of 1 V s^{-1} with a fixed bias voltage between the two electrodes. The current was recorded until the junction broke, at a sampling rate of 10 kHz. When the junction broke, another break junction process was started to form the single-molecule junction for further conductance–electrode potential measurements. Because the measured current from the forward sweeping represents the total contribution from the Faradaic current from electrochemical charging and the tunnelling current from the molecular junctions, only the backward sweep was used to plot the 2D intensity histograms for the molecules. Hundreds of individual curves with mean conductance between 10^{-4} and $10^{-6}G_0$ were selected for further statistics analysis. The 2D histograms of the conductance–electrode potential were constructed with a bin size of 500 × 500 in 2D space.

Current/conductance–voltage measurements. Current/conductance–voltage measurements were carried out under the same environmental conditions as used for the electrochemically gated conductance measurements. Instead of the fixed bias used in the electrochemically gated conductance measurement, a bias between −1.0 V and +1.0 V was continuously swept at a sweeping rate of 5 V s^{-1}. The conductance at 100 mV was used as feedback to control the piezo movement for the repeated opening and closing process, as reported in our previous paper[24,32]. The stretching rate was reduced to ~0.1 nm s^{-1}, and several individual traces were collected from each break junction cycle with a sampling rate of 10 kHz. The low-bias conductance of the current/conductance–voltage curves was determined from the data within the range from −100 mV to 100 mV. 2D histograms of conductance versus voltage were constructed with a bin size of 1,000 × 1,000 in 2D space and the bin size of the conductance distributions of low-bias conductance was $0.03\log(G/G_0)$.

Theoretical calculations. Theoretical calculations were performed with a combination of the ab initio DFT package SIESTA and the quantum transport code Gollum. Due to electrochemical gating, the concentration of the charge double layer formed by positively charged 1-hexyl-3-methylimidazolium (HMI) and negatively charged hexafluorophosphate (PF_6) varied around the molecular backbone; this also changes the local electric field applied to the backbone. Depending on the electrode potentials, either the positively or negatively charged ends of $HMIPF_6$ are oriented towards the backbone. We accounted for the variation in the effective electric field by moving the $HMIPF_6$ with fixed orientation towards the backbone. Figure 4 shows two different configurations of **2,4-TP-SAc** molecular junctions in the presence of $HMIPF_6$, in which the negative or positive region of $HMIPF_6$ is closer to the backbone to simulate the electrochemical gating at positive and negative potentials. We calculated the material specific mean field Hamiltonian[33] of each structure (Supplementary Fig. 9) and then combined it with the quantum transport code Gollum[29] to calculate the transmission coefficient $T(E)$ of electrons with energy E passing from one electrode to the other. The electrical conductance G was then calculated from transmission coefficient $G = G_0T(E_F)$ where E_F is the Fermi energy of the electrodes (see Supplementary Section 5 for details). The conductance for different bias voltages can also be calculated from $G = I/V$ where $I(V) = \int \mathrm{d}E\,T(E)\left(f\left(E-\frac{eV}{2}\right)-f\left(E+\frac{eV}{2}\right)\right)$ and f is the Fermi–Dirac distribution function[28]. To calculate the current/conductance–voltage characteristic of junctions in the linear response regime, the zero-bias transmission coefficient $T(E)$ was combined with the Landauer formula[28].

Data availability

The data that support the findings of this study are available from the corresponding author upon reasonable request.

References

30. Shitanda, I., Kiryu, H. & Itagaki, M. Improvement in the long-term stability of screen-printed planar type solid-state Ag/AgCl reference electrode by introducing poly(dimethylsiloxane) liquid junction. *Electrochim. Acta* **58**, 528–531 (2011).
31. Meszaros, G., Li, C., Pobelov, I. & Wandlowski, T. Current measurements in a wide dynamic range—applications in electrochemical nanotechnology. *Nanotechnology* **18**, 424004 (2007).
32. Hong, W. et al. An MCBJ case study: the influence of π-conjugation on the single-molecule conductance at a solid/liquid interface. *Beilstein J. Nanotechnol.* **2**, 699–713 (2011).
33. José, M. S. et al. The SIESTA method for ab initio order-*N* materials simulation. *J. Phys. Condens. Matter* **14**, 2745–2779 (2002).